

Contents

1. Introduction	1
2. Literature study	2
3. System overview	3
3.1. Hardware	3
3.2. Software	3
4. Modelling	4
4.1. Coordinate frames	4
4.2. States	4
4.3. Forces and moments	4
4.4. Lagrangian mechanics	4
4.5. Linearised model	4
4.6. Discretised model	4
4.7. Model verification	4
4.8. Dynamic payloads	4
5. System identification	5
5.1. White-box and black-box techniques	5
5.1.1. White-box techniques	5
5.1.2. Black-box techniques	6
5.2. Plant considered for system identification	7
5.3. Parameter estimation	8
5.3.1. Payload mass estimation	8
5.3.2. Cable length estimation	9
5.4. Dynamic mode decomposition with control	10
5.5. Hankel alternative view of Koopman	12
5.6. Implementation and results	14
5.6.1. Methodology	15
5.6.2. Error metric	17
5.6.3. Hyperparameters	19
5.6.4. Sample time	21
5.6.5. Choice of payload variable in the state vector	22

5.6.6. Noise	23
5.6.7. System parameters	25
5.6.8. Length of training data	26
5.6.9. Dynamic payload	27
5.7. Conclusion	32
6. Control systems	33
6.1. Cascaded PID	33
6.2. LQR	33
6.3. MPC	33
7. Implementation and results	34
7.1. LQR	34
7.2. MPC	34
7.3. Dynamic payload	34
7.4. System identification with practical data	34
7.5. HIL	34
8. Summary and Conclusion	35
Bibliography	36
A. PID gains	39
B. Random appendix	40

Chapter 1

Introduction

Chapter 2

Literature study

Chapter 3

System overview

3.1. Hardware

3.2. Software

Chapter 4

Modelling

This chapter discusses the mathematical modelling of a quadrotor with a suspended payload which is based on a practical quadrotor UAV named Honeybee. The model is first derived as a 2D model. The system identification and control system techniques in later chapters will then be explained based on the 2D model to avoid unnecessary complexity. Finally, it will be described how this model and the techniques in later chapters are extended to the 3D case. This 3D mathematical model will be used in a nonlinear simulation of a quadrotor and suspended payload. 1

4.1. Coordinate frames

4.2. States

4.3. Forces and moments

4.4. Lagrangian mechanics

4.5. Linearised model

4.6. Discretised model

4.7. Model verification

4.8. Dynamic payloads

water looks like double payload

Chapter 5

System identification

System identification is the process of creating a mathematical model of a dynamical system by using input and output measurements of that system. Two major approaches are used to represent the dynamics of such a system:

1. A priori mathematical modelling with parameter estimation
2. Data-driven system identification

This chapter discusses these system identification approaches and describes the differences between them. For each approach, specific estimation techniques are explained and applied to the quadrotor and payload system. The results of these techniques are then compared to each other.

5.1. White-box and black-box techniques

Models determined from data-driven system identification methods are generally called black-box models. The user is only concerned with the inputs and output of the model and does not determine mathematical relationships from theoretical deductions. In contrast, white-box models are determined from a priori modelling. The user understands the physics of white-box models because the dynamics are manually programmed into the model by the user.

5.1.1. White-box techniques

The underlying physics of a white-box model is understood by the user because it is determined from first principles. This is done by modelling physical processes with techniques like Lagrangian mechanics or Newton equations. For system identification techniques that use these models, the mathematical relations between system parameters are predefined in the modelling phase. The system identification process is therefore reduced to parameter estimation which determines values for the parameters used in the model.

This approach is used by [1] and [2] for swing damping control of a quadrotor with an unknown suspended payload. The system was modelled as two rigid bodies connected by a link and the following assumptions were made regarding the suspended payload:

- The payload is a point mass.
- The link is massless.
- The link is rigid.
- The link is attached to the CoM of the quadrotor.

The only unknown parameters in the quadrotor and payload model is the payload mass and the link length. These parameters are first estimated and then inserted into the predefined, linearised model. This model is used by a LQR controller to damp swing angles while also controlling the vehicle.

The approach works well for systems with predictable dynamics, but is not very adaptable to systems with slightly different dynamics. The payload considered by [1] and [2] is limited to a small rigid mass suspended from the quadrotor by a non-stretching cable. In this configuration it was shown that a LQR controller successfully controls a quadrotor while minimising payload swing angles. However, if a payload or cable is used that violates one of the modelling assumptions, the predefined model no longer accurately represent the system. Many payloads which are considered for practical drone deliveries do not conform to these assumptions. Since the controller is dependent on this model, the mismatch between the model and actual dynamics may result in undesirable controller behaviour.

5.1.2. Black-box techniques

Data-driven system identification methods produce black-box models. These models do not require predefined mathematical relations between system parameters. No prior knowledge of the physics of the system are considered and no modelling assumptions are made. Black-box techniques determine the mathematical relationship between inputs and outputs of a system using information from measurement data only.

Dynamical models can be categorised as either non-linear or linear models. Non-linear models are often more accurate than linear models because complex, real-world dynamics are better approximated by non-linear systems. The dynamics of a quadrotor and suspended payload are also non-linear.

However, non-linear models are inherently more complex than linear models. Controllers based on non-linear models are usually more computationally complex than those with linear models. The control architectures used for quadrotors in practical applications are mostly implemented on onboard hardware. Therefore there is value in low-complexity, linear models because these may be simple enough to execute on low cost hardware. Non-linear models may require control implementations that are too computationally expensive and may not be practically realisable on the available hardware on a quadrotor.

DMDc and HAVOK are the two data-driven system identification methods investigated in this work. These are linear regression techniques that produce linear models to approximate non-linear dynamics. Non-linear data-driven techniques like Neural Networks and SINDy [3] may produce models that are more accurate than linear techniques, but at the cost of greater computational complexity. DMDc and HAVOK are less computationally complex and their models are suitable for linear MPC, which is significantly faster than non-linear MPC. This is desirable for a practical quadrotor implementation, where onboard computational power is limited. These techniques and their implementations are explained in the sections below.

5.2. Plant considered for system identification

Only the North velocity controller will be considered in this section. Because of the symmetry of the quadrotor, this controller can then be duplicated for East velocity control. The resulting input vector of the system identification plant is given by,

$$\mathbf{u} = [A_{N,sp}]^T. \quad (5.1)$$

For swing damping control, the controllers require state feedback from both the quadrotor and payload, hence the state vector of the considered plant is,

$$\mathbf{x} = [V_N \quad \theta \quad \dot{\theta}]^T. \quad (5.2)$$

Note that position is not included in the state vector because it does not affect the velocity controller. Also note that the inner loop controllers handle the attitude dynamics of the quadrotor. During pure longitudinal velocity setpoints the quadrotor experiences negligible altitude changes due to the swinging payload. This is due to speed of the altitude controllers and the weak coupling between the payload angle and the altitude dynamics. The plant seen by the system identification process therefore mimics the common pendulum-on-a-cart model. A schematic of this 2D plant is shown in Figure 5.1. In the following sections, simulations of the full quadrotor and payload system will be performed and different methods will be applied to identify different models of this plant.

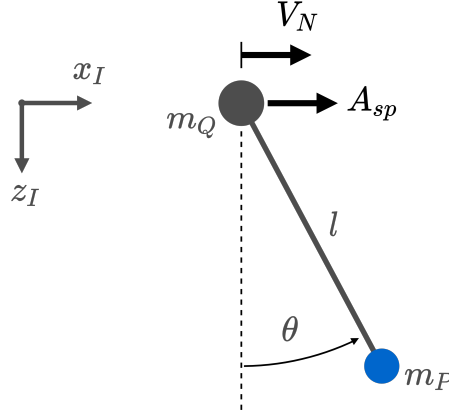


Figure 5.1: Schematic of a floating pendulum model considered for a North velocity controller

5.3. Parameter estimation

The purpose of parameter estimation is to determine unknown values required by a predetermined, white-box model. The identified model is used to design a LQR controller and therefore needs to be in a linear, continuous-time, state-space form. This model was derived and linearised a priori in Section 4.5. The unknown parameters in the model include the payload mass, m_p and the cable length, l . Two separate methods are used to estimate each of these parameters. This method was used by [1] and [2] to design a LQR controller and implement swing damping control of a quadrotor with an unknown suspended payload.

5.3.1. Payload mass estimation

RLS is used by [1] and [2] to estimate the payload mass. It is assumed that the quadrotor mass is known before flight, therefore the payload mass can be estimated from the additional thrust required during hover. In both [1] and [2] it is demonstrated that RLS is very accurate for a system nearly identical to the one considered in this work. To compare other aspects of the white-box and black-box techniques with more clarity, it will therefore be assumed that the method estimates m_p with perfect accuracy. This isolates any inaccuracies in the white-box model to either the a priori modelling or the cable length estimation.

It should be noted however that this method is dependant on the assumption that the vehicle mass is known and remains unchanged. The method will clearly be inaccurate if a unknown mass is added to the quadrotor in conjunction with the suspended payload.

Common practical examples of this include adding a camera to the vehicle or using a different battery for a different flight range. In these cases the mass estimation method will have to be redesigned. This is an inherent problem of the white-box techniques. The parameter estimation methods are designed for specific modelling assumptions and are not adaptable to different types of payload loadings. In contrast, data-driven techniques are adaptable to different payload loadings because it does not depend on a priori modelling assumptions.

5.3.2. Cable length estimation

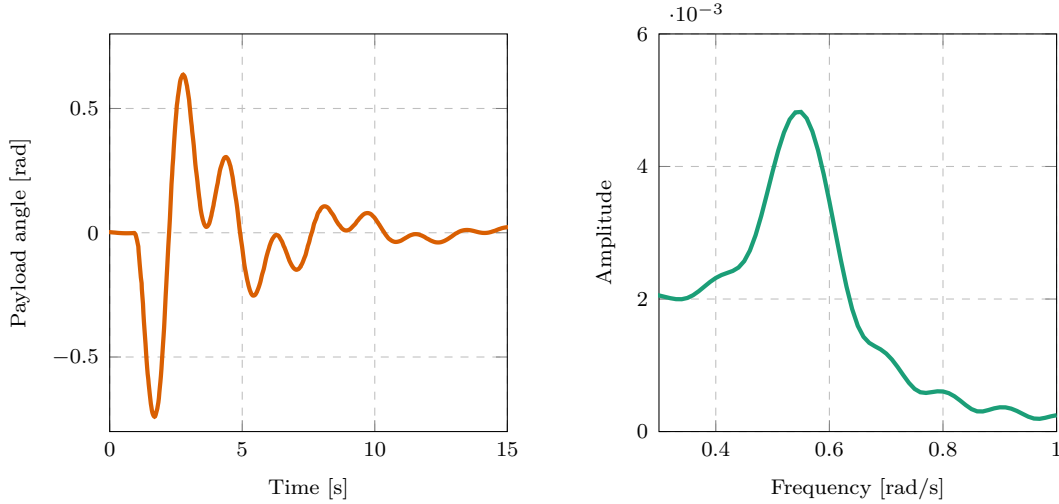
The cable length is estimated from the measurement of the natural frequency of the swinging payload. As described by [4], the natural frequency is given by:

$$\omega_n = \sqrt{\frac{g}{l} \cdot \frac{m_q + m_p}{m_q}}. \quad (5.3)$$

The cable length can clearly be calculated from (5.3) if the other parameters are known. The natural frequency is measured by performing a FFT on the payload swing angle response after a position step by the quadrotor. The dominant frequency identified by the FFT during free swing is an approximate measurement of the natural frequency of the payload. Note that the measured frequency actually corresponds to the damped natural frequency, but it is assumed that damping during free swing is negligible. Therefore the damped natural frequency closely approximates the natural frequency.

Figure 5.2a shows the payload swing angle response to a position step setpoint. The first few seconds of the step response are excluded from the FFT to minimise the effect of the transient response and the quadrotor controllers on the natural frequency measurement. Figure 5.2b shows the resulting single-sided amplitude spectrum of the FFT of this data.

The dominant frequency is clearly identified by the peak at 0.520 rad/s. Since m_q , m_p and g are known, and ω_n has been measured, l can be determined from (5.3). The estimated length for this simulation is 0.953 m. The actual cable length is 1 m, therefore this estimation has an error of 4.7%. As documented [1] and [2], an error of this magnitude is acceptably small and still results in effective control with a LQR. It is also shown by [1] and [2] that this estimation method is effective for a range of different payloads.



(a) Position step response of the payload swing angle (b) The single-sided amplitude spectrum of the FFT

Figure 5.2: Data from a position step response used for cable length estimation ($l = 1$ m, $m_p = 0.3$ kg.).

5.4. Dynamic mode decomposition with control

DMD is a regression technique that can be used to approximate a non-linear dynamical system with a linear model [5]. It uses temporal measurements of system outputs to reconstruct system dynamics without prior modelling assumptions. DMDc is an adaptation of DMD that also accounts for control inputs [6]. This section provides an overview of the specific implementation of DMDc used in this work. Note that this implementation is an adaptation of DMDc, and includes time-delay-embedding of multiple observables. Enriching a DMD model with time-delay-embedding is a known technique and is also seen in other DMD adaptations [7, 8].

DMD produces a linear, discrete state-space model of system dynamics. Discrete measurements, \mathbf{x}_k , of the continuous time observable, $\mathbf{x}(t)$, are used, where $\mathbf{x}_k = \mathbf{x}(kT_s)$, and T_s is the sampling time of the model. Delay-coordinates (i.e. \mathbf{x}_{k-1} , \mathbf{x}_{k-2} , etc.) are also included in the state-space model to account for input delay and state delay in the system. Input delay refers to the time delay involved with transporting a control signal to a system, whereas state delay refers to time-separated interactions between system variables [9]. Hence, we define an state delay vector as:

$$\mathbf{d}_k = [\mathbf{x}_{k-1} \quad \mathbf{x}_{k-2} \quad \cdots \quad \mathbf{x}_{k-q+1}]^T, \quad (5.4)$$

$\mathbf{d}_k \in \mathbb{R}^{(n_x)(q-1)}$ and where q is the number of delay-coordinates (including the current time-step) used in the model.

The discrete state-space model is therefore defined as:

$$\mathbf{x}_{k+1} = \mathbf{A}\mathbf{x}_k + \mathbf{A}_d\mathbf{d}_k + \mathbf{B}\mathbf{u}_k, \quad (5.5)$$

$\mathbf{A} \in \mathbb{R}^{n_x \times n_x}$ is the system matrix, $\mathbf{A}_1 \in \mathbb{R}^{(q-1) \cdot n_x \times (q-1) \cdot n_x}$ is the state delay system matrix and $\mathbf{B} \in \mathbb{R}^{n_x \times n_u}$ is the input matrix.

The training data consists of full-state measurements, \mathbf{x}_k , and corresponding inputs, \mathbf{u}_k , taken at regular intervals of $\Delta t = T_s$, during a simulated flight with Cascaded PID control. In a practical flight, these time-series measurements need to be saved in memory because it is used as a single batch by DMD. Note that DMD can be applied in a recursive manner as described in [10], However this implementation is not considered because memory size will not be a limitation since a companion computer will be used.

The training data is collected into the following matrices:

$$\begin{aligned} \mathbf{X}' &= \begin{bmatrix} \mathbf{x}_{q+1} & \mathbf{x}_{q+2} & \mathbf{x}_{q+3} & \cdots & \mathbf{x}_{w+q} \end{bmatrix}, \\ \mathbf{X} &= \begin{bmatrix} \mathbf{x}_q & \mathbf{x}_{q+1} & \mathbf{x}_{q+2} & \cdots & \mathbf{x}_{w+q-1} \end{bmatrix}, \\ \mathbf{X}_d &= \begin{bmatrix} \mathbf{x}_{q-1} & \mathbf{x}_{q+0} & \mathbf{x}_{q+1} & \cdots & \mathbf{x}_{w+q-2} \\ \vdots & \vdots & \vdots & \ddots & \vdots \\ \mathbf{x}_2 & \mathbf{x}_3 & \mathbf{x}_4 & \cdots & \mathbf{x}_{w+1} \\ \mathbf{x}_1 & \mathbf{x}_2 & \mathbf{x}_3 & \cdots & \mathbf{x}_w \end{bmatrix}, \\ \mathbf{\Upsilon} &= \begin{bmatrix} \mathbf{u}_q & \mathbf{u}_{q+1} & \mathbf{u}_{q+2} & \cdots & \mathbf{u}_{w+q-1} \end{bmatrix}, \end{aligned} \quad (5.6)$$

where w is the number of columns in the matrices, \mathbf{X}' is the matrix \mathbf{X} shifted forward by one time-step, \mathbf{X}_d is the matrix with delay states, and $\mathbf{\Upsilon}$ is the matrix of inputs. Equation (5.5) can be combined with the matrices in Equation (5.6) to produce:

$$\mathbf{X}' = \mathbf{A}\mathbf{X} + \mathbf{A}_d\mathbf{X}_d + \mathbf{B}\mathbf{\Upsilon}. \quad (5.7)$$

Note that the primary objective of DMDc is to determine the best fit model matrices, \mathbf{A} , \mathbf{A}_d and \mathbf{B} , given the data in \mathbf{X}' , \mathbf{X} , \mathbf{X}_d , and $\mathbf{\Upsilon}$ [6]. In order to group the unknowns into a single matrix, (5.5) is manipulated into the form,

$$\mathbf{X}' = \begin{bmatrix} \mathbf{A} & \mathbf{A}_d & \mathbf{B} \end{bmatrix} \begin{bmatrix} \mathbf{X} \\ \mathbf{X}_d \\ \mathbf{\Upsilon} \end{bmatrix} = \mathbf{G}\mathbf{\Omega}, \quad (5.8)$$

where $\mathbf{\Omega}$ contains the state and control data, and \mathbf{G} represents the system and input matrices.

A SVD is performed on $\mathbf{\Omega}$ resulting in: $\mathbf{\Omega} = \mathbf{U}\mathbf{\Sigma}\mathbf{V}^T$. Often, only the first p columns of \mathbf{U} and \mathbf{V} are required for a good approximation of the dynamics [11]. In many cases, the truncated form results in better models than the exact form when noisy measurements are used. This is because the effect of measurement noise is mostly captured by the truncated columns of \mathbf{U} and \mathbf{V} . By truncating these columns, the influence of noise in the regression problem is reduced. Hence the SVD is used in the truncated form:

$$\mathbf{\Omega} \approx \tilde{\mathbf{U}}\tilde{\mathbf{\Sigma}}\tilde{\mathbf{V}}^T, \quad (5.9)$$

where \sim represents rank- p truncation.

By combining (5.9) with the over-constrained equality in (5.8), the least-squared solution, \mathbf{G} , can be found with:

$$\mathbf{G} \approx \mathbf{X}'\tilde{\mathbf{V}}\tilde{\mathbf{\Sigma}}^{-1}\tilde{\mathbf{U}}. \quad (5.10)$$

By reversing 5.8, \mathbf{G} can now be separated into: $\mathbf{G} = [\mathbf{A} \quad \mathbf{A}_d \quad \mathbf{B}]$. according to the required dimensions of each matrix. Thereby, the state-space model approximated by DMDc is complete.

5.5. Hankel alternative view of Koopman

HAVOK is a data-driven, regression technique that provides a connection between DMD and Koopman operator theory [11,12]. We have adapted the standard HAVOK algorithm slightly to account for the effect of control and to extract a discrete, linear model that approximates the behaviour of a controlled dynamical system. In this section, a brief overview is provided for this implementation and adaptation of HAVOK.

A defining characteristic of HAVOK is that it uses multiple delay-coordinates (i.e. $\mathbf{x}_{k-1}, \mathbf{x}_{k-2}$, etc.) in the system identification process. To fit this into the standard state-space format, an extended state vector is defined as:

$$\mathbf{a}_k = [\mathbf{x}_{k-(q-1)} \quad \cdots \quad \mathbf{x}_{k-1} \quad \mathbf{x}_k]^T, \quad (5.11)$$

where $\mathbf{a}_k \in \mathbb{R}^{(n_y)(q)}$, and the subscript of \mathbf{a} denotes the highest subscript of \mathbf{x} in the vector.

The resulting discrete state-space model is therefore in the form,

$$\mathbf{a}_{k+1} = \tilde{\mathbf{A}}\mathbf{a}_k + \tilde{\mathbf{B}}\mathbf{u}_k, \quad (5.12)$$

where $\tilde{\mathbf{A}} \in \mathbb{R}^{(q \cdot n_x) \times (q \cdot n_x)}$ is the system matrix, and $\tilde{\mathbf{B}} \in \mathbb{R}^{(q \cdot n_x) \times n_u}$ is the input matrix. Here, \sim is used to differentiate these matrices from \mathbf{A} and \mathbf{B} used in DMDc.

The original HAVOK algorithm, developed by [13], constructs a Hankel matrix from output variables only. In this work, the standard HAVOK algorithm has been adapted to incorporate the effect of control. An extended Hankel matrix, $\mathbf{\Pi}$, is created by appending a matrix of inputs to a Hankel matrix of measurements:

$$\mathbf{\Pi} = \begin{bmatrix} \mathbf{a}_q & \mathbf{a}_{q+1} & \mathbf{a}_{q+2} & \cdots & \mathbf{a}_{w+q-1} \\ \mathbf{u}_q & \mathbf{u}_{q+1} & \mathbf{u}_{q+2} & \cdots & \mathbf{u}_{w+q-1} \end{bmatrix}, \quad (5.13)$$

where w is the number of columns in $\mathbf{\Pi}$. A truncated SVD of this Hankel matrix results in following approximation:

$$\mathbf{\Pi} \approx \tilde{\mathbf{U}} \tilde{\mathbf{\Sigma}} \tilde{\mathbf{V}}^T, \quad (5.14)$$

where \sim represents rank- p truncation. It is important to note that the model extracted by HAVOK depends on the choice of hyperparameters (p and q), and the number of training samples ($N_{train} = w + q - 1$).

The columns of $\tilde{\mathbf{V}}$ are the most significant principal components of the system dynamics [14]. This matrix, $\tilde{\mathbf{V}}$, can be considered to contain a time-series of the pseudo-state, \mathbf{v} , such that $\tilde{\mathbf{V}}^T = [\mathbf{v}_q \ \mathbf{v}_{q+1} \ \cdots \ \mathbf{v}_w]$, characterises the evolution of the actual dynamics in an eigen-time-delay coordinate system [13]. Consider the following discrete, state-space formulation:

$$\mathbf{v}_{k+1} = \mathbf{\Lambda} \mathbf{v}_k. \quad (5.15)$$

HAVOK determines the best fit linear operator $\mathbf{\Lambda}$ that maps the pseudo-state \mathbf{v}_k to \mathbf{v}_{k+1} . In order to setup an over-determined equality for (5.15), $\tilde{\mathbf{V}}^T$ is divided into two matrices:

$$\begin{aligned} \mathbf{V}_1 &= \begin{bmatrix} \mathbf{v}_q & \mathbf{v}_{q+1} & \cdots & \mathbf{v}_{w-1} \end{bmatrix}, \\ \mathbf{V}_2 &= \begin{bmatrix} \mathbf{v}_{q+1} & \mathbf{v}_{q+2} & \cdots & \mathbf{v}_w \end{bmatrix}, \end{aligned} \quad (5.16)$$

where \mathbf{V}_2 is \mathbf{V}_1 advanced a single step forward in time. The matrices from Equation (5.16) are now combined with Equation (5.15) and the best fit $\mathbf{\Lambda}$ is determined with the Moore-Penrose pseudoinverse:

$$\mathbf{V}_2 = \mathbf{\Lambda} \mathbf{V}_1 \quad \Rightarrow \quad \mathbf{\Lambda} \approx \mathbf{V}_1 \mathbf{V}_1^\dagger \quad (5.17)$$

It can be shown from Equation (5.14) that Equation (5.15) is transformed from the eigen-time-delay coordinate system to the original coordinate system as the following:

$$\begin{bmatrix} \mathbf{a}_{k+1} \\ \mathbf{u}_{k+1} \end{bmatrix} = (\tilde{\mathbf{U}} \tilde{\mathbf{\Sigma}}) \mathbf{\Lambda} (\tilde{\mathbf{U}} \tilde{\mathbf{\Sigma}})^\dagger \begin{bmatrix} \mathbf{a}_k \\ \mathbf{u}_k \end{bmatrix}. \quad (5.18)$$

$\tilde{\mathbf{A}}$ and $\tilde{\mathbf{B}}$ can now be extracted from the matrix, $(\tilde{\mathbf{U}}\tilde{\mathbf{\Sigma}})\mathbf{\Lambda}(\tilde{\mathbf{U}}\tilde{\mathbf{\Sigma}})^\dagger$. This extraction is illustrated in Figure 5.3, where different blocks represent different groups of matrix entries.

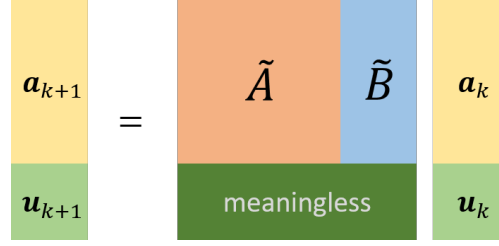


Figure 5.3: Illustration of the extraction of $\tilde{\mathbf{A}}$ and $\tilde{\mathbf{B}}$ from (5.18)

Note that the matrix entries in Figure 5.3 that map \mathbf{u}_k to \mathbf{u}_{k+1} are meaningless for state predictions and are discarded. Also note that the state vector, \mathbf{a}_k , includes delay-coordinates, therefore some matrix entries are independent of the dynamics. This is illustrated in Figure 5.4 for an example model with $q = 4$. For example, the mapping of \mathbf{x}_k in the state vector to \mathbf{x}_k in the predicted state vector corresponds to a entry of 1 in the $\tilde{\mathbf{A}}$ matrix. This is fixed by the model format and is not a function of the system dynamics. Due to the least-squares fitting and the coordinate transformation of the algorithm, HAVOK does not produce these exact values in $\tilde{\mathbf{A}}$ and $\tilde{\mathbf{B}}$. By forcing each of these matrix entries to 1 or 0, the state-prediction performance of the model is improved.

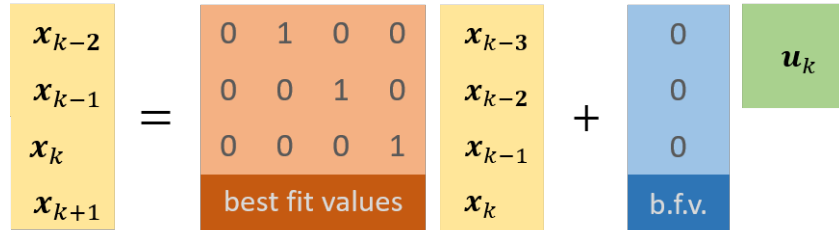


Figure 5.4: Illustration of

Finally, the improved $\tilde{\mathbf{A}}$ and $\tilde{\mathbf{B}}$ are inserted into (5.12) to render the HAVOK model.

5.6. Implementation and results

Numerous simulations were performed with different system configurations to investigate the performance of these system identification techniques. Firstly, the influence of design parameters on the algorithm performance will be discussed. These parameters include hyperparameters, the length of training data and the algorithm sample time. The effect of conditions that are not determined by algorithm design will also be explored, like measurement noise, and the physical properties of the payload. Finally, the white-box

and black-box techniques will be tested on a dynamic payload which does not satisfy the assumptions of a simple pendulum.

5.6.1. Methodology

A SITL implementation of PX4 [15] using the Gazebo simulator [16] is used to generate data for system identification. Testing these techniques with simulation data allow us to investigate a much larger range system configurations than possible with practical flights. The simulation model used in Gazebo was verified in Chapter 4. Using PX4 in SITL also ensures that the controller dynamics in simulation is as close as possible to practical flights since the same flight stack is used in both cases. Gazebo also applies realistic measurement noise to the signals received by PX4, which applies an EKF for state estimation. Therefore the the data seen by the system identification techniques will also include the filtering effect of the EKF as it would in practical flights.

The procedure used to evaluate the black-box techniques is as follows:

1. Takeoff and hover with the quadrotor
2. Start logging input and output data
3. Command a series of velocity step setpoints with random step sizes and time intervals
4. Stop logging data
5. Split data into separate training and testing periods
6. Build a model from the training data
7. Calculate a error metric for the model from the testing data

The default PID velocity controller from PX4 is used during these simulation. The implemented controller gains are documented in Appendix A. A ROS node is used to read and log the payload angle measurement from Gazebo and a different ROS node is used to send the velocity setpoints to PX4 through the MAVLink protocol with the ROS package, 'mavros'.

A algorithm schedules the series of velocity step commands by assigning random step values and time-intervals within a specified range. Theses values are selected from a uniform distribution within the ranges specified in Table 5.1 The maximum velocity step is determined in simulation by iteratively increasing the maximum velocity step to a safe value where the quadrotor remains in stable flight and the payload angles do not swing out of control. The time interval range is set iteratively to ensure that the generated data includes both transient and steady-state dynamics.

Table 5.1: Input data ranges.

	Velocity step [m/s]	Step time interval [s]
Minimum	0	10
Maximum	3	25

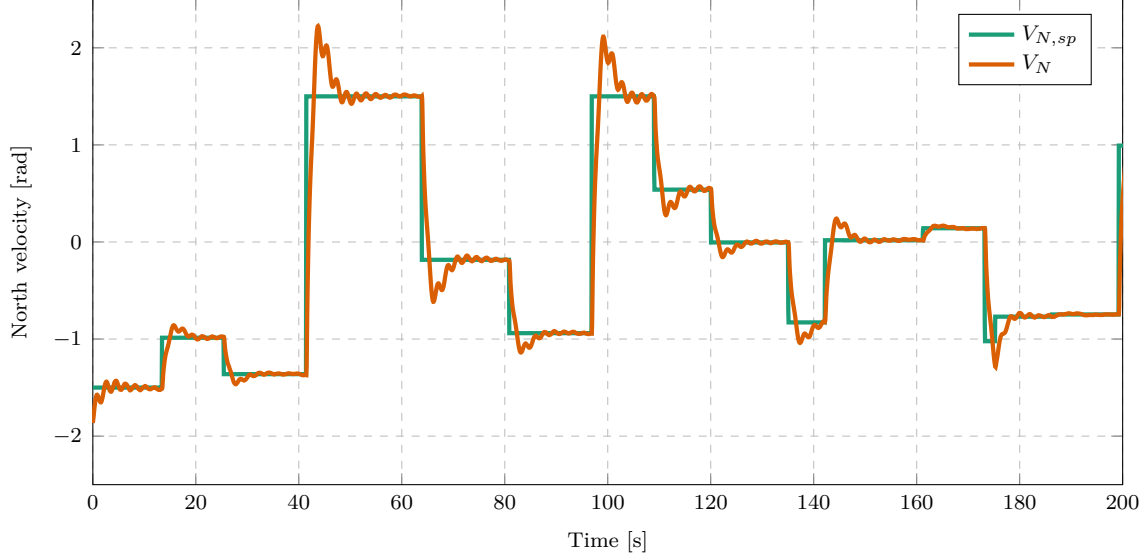
**Figure 5.5:** Example of training data with random velocity step inputs ($m = 0.2\text{ kg}$, $l = 1\text{ m}$)

Figure 5.5 shows an example of random velocity steps and the resulting velocity response used as training data. Using random velocity steps and time intervals prevents the system identification methods from overfitting to a specific set of control conditions. The method should rather determine a generalised model that works over a range of possible control conditions.

The data logged from simulation is then divided into testing and training data. The training data is used by the system identification algorithms to generate a regression model and the model is then used to determine a prediction error metric over the unseen testing data. It is common practice in model evaluations to use separate sets of data for training and testing. This ensures that good predictions scores do not result from models that overfit to the training data.

The testing data spans a fixed length of time and taken from the start of the simulation period. The training data is then allocated from the remainder of the data. The same testing data is used to calculate error metrics for different models with different configurations to ensure that the metric for each model is comparable. This error metric calculated from the testing data is used to evaluate and rank the performances of different models.

5.6.2. Error metric

It is common practice is to select a model for a MPC based on k-step-ahead prediction errors [17]. This is because the model is used to make k-step-ahead predictions during control optimisation. When model error is dominated by variance error (caused by disturbances), it may be better to use one-step-prediction error [17]. However for the quadrotor and payload case it is assumed that variance error (caused by under modelling) dominates the model error.

Different metrics are used in literature to quantify prediction accuracy for different applications. Very common, scale-dependant error metrics are MSE and MAE. These metrics are dependant on the unit and scale of a variable, hence they cannot be used to compare predictions of different variables. MSE (l_2 norm of error values) penalises larger errors more than smaller errors, whereas MAE (l_1 norm) penalises errors equally. For our use case the l_1 norm provides a more intuitive metric than the l_2 norm because it has the same unit as the prediction variable and there is no motivation to penalise larger errors more than smaller errors for our use case.

MAE is calculated as:

$$\mathbf{MAE} = \text{mean} (|\hat{\mathbf{x}}_k - \mathbf{x}_k|), \quad (5.19)$$

where \mathbf{x}_k is the actual state vector at time-step k , $\hat{\mathbf{x}}_k$ is the state prediction, and \mathbf{MAE} is a vector with the MAE of each state.

Popular, scale-free error metrics, like MAPE, MRAE and MASE, are also based on the l_1 norm, but are independent of the scale and units of a variable [18]. These metrics could therefore be used to compare predictions of different variables. However, these metrics provide misleading comparisons for our use case. MAPE expresses accuracy as the absolute ratio between the error and actual value at each time-step. This results in undefined or extremely large values for the payload angle predictions because the state has a zero mean. The velocity state variable has a non-zero mean, therefore the scale of the MAPE of velocity will significantly different from the MAPE of the payload angle.

MRAE is also popular metric for comparing predictions models used with a MPC [19], however, similarly to MAPE, it also results in undefined values for the payload swing angle. MASE does not have this problem and can compare predictions of different variables well, because it expresses accuracy as the ratio between the MAE of the model prediction and the MAE of an in-sample naïve forecast [18]. However, an in-sample forecast is a naïve prediction for a one-step-ahead prediction, but not for a k-step-ahead prediction. Therefore MASE is not a helpful ratio for our use case.

$NMAE_{mm}$ is a scale-free error metric that can compare different variables in our use case. It normalises the MAE of a variable by the range of that variable, thereby variables with different means or scales can be compared. This value is calculated as:

$$NMAE_{mm} = \frac{MAE}{x_{max} - x_{min}} \quad (5.20)$$

where $x_{i,max}$ and $x_{i,min}$ are the maximum and minimum values of the considered variable in the testing data.

This results in an error metric for each predicted variable, but a single value is required per model to rank the overall accuracy of different models. Therefore the average of the $NMAE_{mm}$ of all state variables is used as the single value representing the overall accuracy of a model. This is the final error metric used to evaluate the model predictions in the sections to follow.

Other criteria which are more statistically rigorous in model selection than error metrics are AIC and BIC scores. Thereby they provide a quantitative way of performing a Pareto analysis, which balances model complexity with model accuracy [20]. It is generally advantageous to use a parsimonious model, which has a low prediction error but is not overly complex, than a complex model with a slightly lower prediction error. This not only helps to avoid overfitting, but also ensures that the MPC optimisation problem is not too computational expensive for the available hardware. However, these scores require the computation of the maximum log likelihood of each model over numerous simulations. This is computationally intractable and unpractical for our use case because of the large number of hyperparameter combinations to compare, as explained in Section 5.6.3. Therefore an error metric will rather be used to evaluate model accuracy.

The error metric of one model may change significantly different starting conditions or prediction horizons. The prediction horizon used for model analysis is selected as 20 s which is at least twice as long as the desired MPC prediction horizon. Some models have very accurate transient predictions, but prove to be unstable over a longer time horizon. If the prediction horizon is too short, these models may score unreasonably low error metrics. Selecting these such a model could result in unstable control at certain control conditions. Therefore a long prediction horizon is used for testing so that marginally unstable models are penalised heavily in model selection.

Different starting conditions also have a large influence on the prediction score of a model. Some models may accurately predict transient behaviour, while being extremely bad at steady-state predictions. This would result in an MPC controlling the plant well during

the initial step response, but becoming unstable during steady-state control. In order to have a MPC that can control the plant during the different stages of a flight, a model needs to be selected with accurate predictions over a range of different control conditions.

Therefore the error metric needs to include predictions from multiple starting conditions in the testing data. The resulting testing procedure is to first specify a number of equispaced starting conditions within the testing data. The model is then run multiple times for the length of the prediction horizon, starting with different initial conditions each time. The NMAE_{mm} is determined for each run, whereafter the average of these scores gives the final NMAE_{mm} score of the model. In order to balance the variety of testing conditions with the computational time per error metric calculation, 10 was selected as the number of initial conditions used in the final NMAE_{mm} score.

5.6.3. Hyperparameters

As discussed in Section 5.4 and 5.5 DMDc and HAVOK models are dependent on two hyperparameters: the number of delay-coordinates, q , and the SVD truncation rank, p . For each system identification run with different system parameters or a different length of training data, a hyperparameter search is performed to find the combination of hyperparameters that results the lowest prediction error. Firstly, a coarsely spaced grid search is performed with large intervals between tested hyperparameter values. The range of tested hyperparameters is then reduced and a finer hyperparameter search is performed. From numerous simulation iterations, the range of significant hyperparameter values is conservatively determined to be,

$$5 < q < 30, \quad 5 < p < 50 \quad (5.21)$$

Figure 5.6 shows the prediction error of DMDc and HAVOK models for different values of q . For each value of a q , a new model is generated with every p in the considered range and the lowest prediction error is plotted. There is only a slight difference between the results of DMDc and HAVOK. As expected, the models with the least number of terms have the highest prediction errors. As the number of terms available to the model increases, the error decreases. It is clear that there is a sharp decrease in prediction error for $2 < q < 6$, however there is no longer a significant decrease in error as model complexity increases past $q > 12$.

This ‘elbow’ in the plot can be considered as the Pareto front, where there is a balance between model complexity and accuracy [20]. It is desirable to select a parsimonious

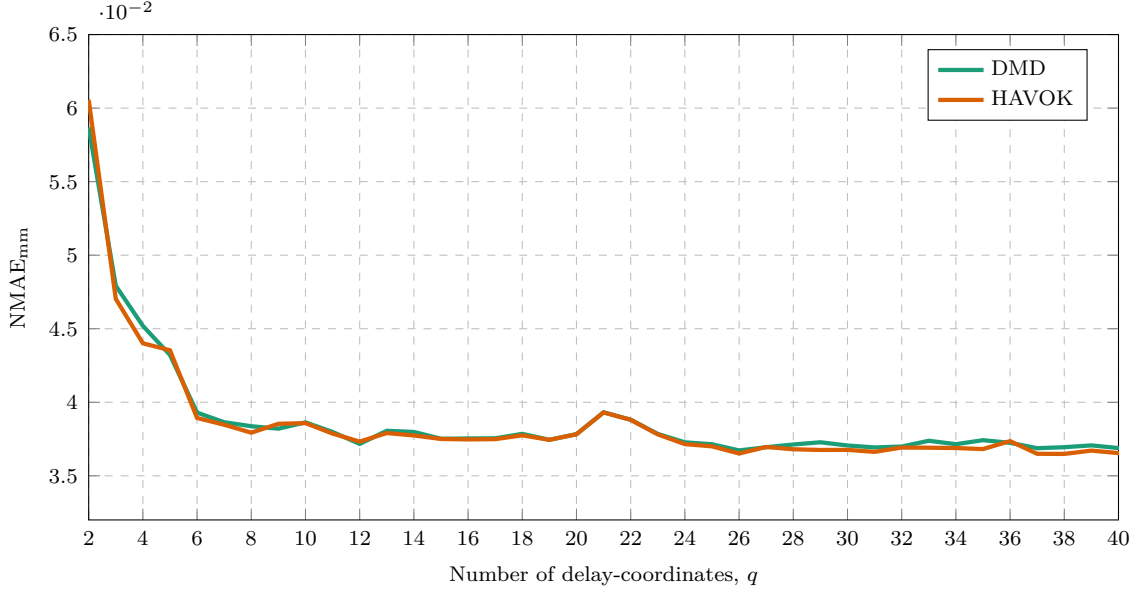


Figure 5.6: DMD and HAVOK predictions error for different lengths of noisy training data ($m = 0.2$ kg, $l = 0.5$ m, $T_s = 0.03$ s, $T_{train} = 60$ s.)

model on this front that has just enough free parameters to capture the plant dynamics and have good accuracy, without being overly complex [21]. These models are less prone to overfitting and also lead to lower computational complexity in the MPC optimisation problem.

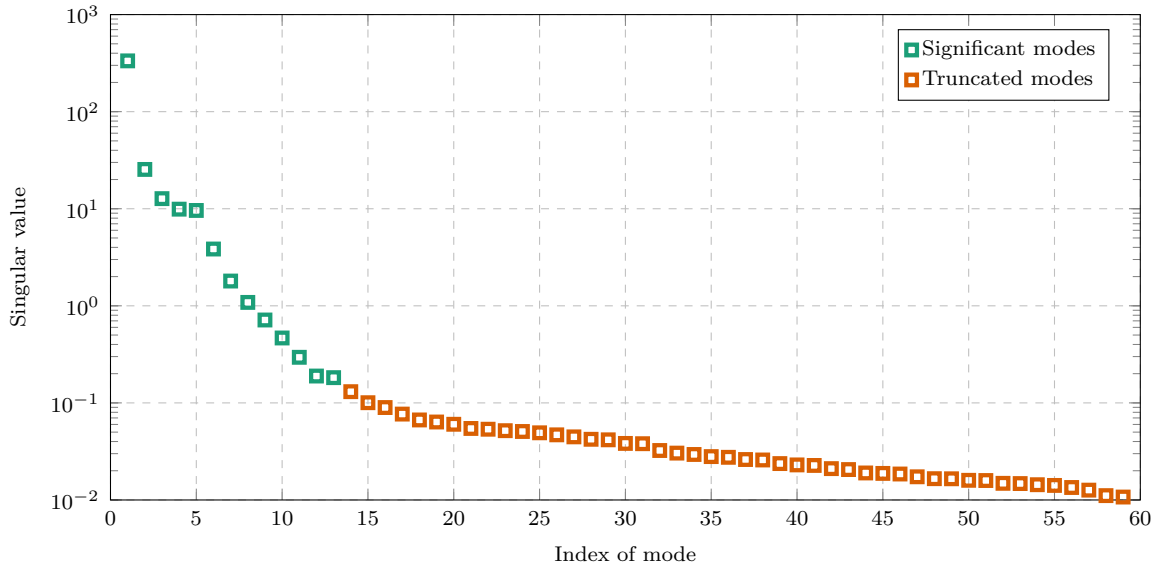


Figure 5.7: Significant and truncated singular values of a HAVOK model produced from noisy data ($m = 0.2$ kg, $l = 0.5$ m, $T_s = 0.03$ s, $T_{train} = 60$ s.)

Figure 5.7 plots the singular values of the SVD from a HAVOK model in a log scale. The singular values of the SVD can be loosely interpreted as a measure of significance of the corresponding POD mode to the plant dynamics [22]. That is, modes with higher singular

values contain more relevant information about the plant dynamics than modes with lower singular values. The p number of significant singular values, which correspond to the POD modes used to reconstruct the observed dynamics, are specifically shown in the plot. The truncated singular values are also shown, which correspond to the discarded modes.

The Pareto ‘elbow’ is also visible in this plot where there is noticeable change in gradient roughly at the split between significant and truncated values. This change in gradient shows that after p modes, there is a significant drop in information contributed per remaining mode. Note that the number p was selected from a hyperparameter search using an error metric which did not consider the singular values. This seems to confirm the notion that the Pareto optimal solution is often the most accurate representation of the actual dynamics [22].

5.6.4. Sample time

The sample time, T_s , used for system identification is the sample time of the discrete model, which determines the sample time of the MPC. Resampling strategies can enable the MPC to run at a different frequency to the discrete model but this adds unnecessary complexity to the control architecture.

The MPC acts in the velocity loop and commands an acceleration setpoint. The default PID velocity controller runs at 50 Hz which corresponds to $T_s = 0.02$ s. Due to the computational complexity of an MPC, the optimiser will struggle to run at 50 Hz on a companion computer on a quadrotor. However, the controller needs to run as fast as possible to have significant time-scale separation from the quadrotor dynamics. If the controller runs too slowly, it may result in poor flight performance or unstable control. The highest natural frequency of the payload based on the range of physical parameters considered is 8.39 Hz corresponding to a period of 0.119 s.

Figure 5.8 shows the prediction error of different DMD models generated with a range of different sample times. The natural frequency of the payload pendulum is dependant on the cable length and influences the frequency response of the plant. Therefore Figure 5.8 plots the experiment result for different cable lengths to see if it has an effect on the prediction error of the models.

Note that for all considered cable lengths, the prediction error has a sharp decrease for $T_s > 0.045$ s. This may be because the model does not try to capture the small, high frequency oscillations in the dynamics at such slow sample times. Hence the long term prediction of the models fits the general shape of the dynamics well and results in low errors. However, this sample time is too slow for controlling the practical quadrotor.

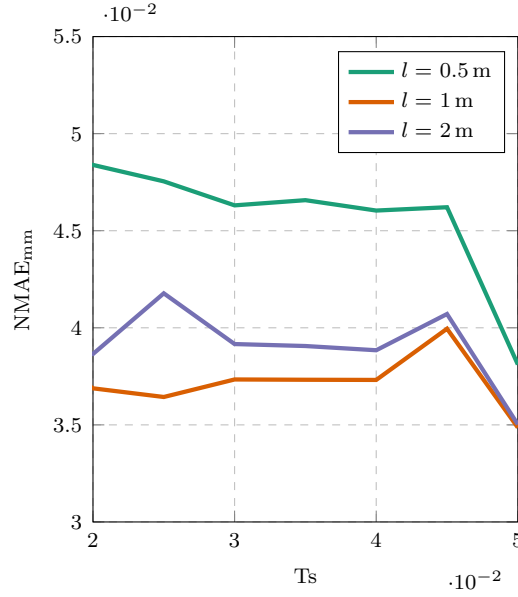


Figure 5.8: DMD prediction error using different cable lengths with a range of different sample times of noisy training data ($m = 0.2$ kg)

$T_s = 0.03$ s is selected as the sample time for system identification because it provides a good balance between being fast enough for the quadrotor dynamics and slow enough for a practical MPC implementation.

5.6.5. Choice of payload variable in the state vector

As discussed in Section 5.2, the equations of motion in continuous-time of a floating pendulum are dependent on $\dot{\theta}$ and V_N , but are not dependent on θ . Therefore it is expected that $\mathbf{x} = [V_N \ \dot{\theta}]^T$ will be used as the state vector for system identification. However, if $\dot{\theta}$ is not included in the state vector of a discrete model, it can still be represented with numerical differentiation of θ . An example of this is the backward Euler form,

$$\dot{\theta}_k = \left(\frac{1}{T_s}\right) \cdot \theta_k - \left(\frac{1}{T_s}\right) \cdot \theta_{k-1}. \quad (5.22)$$

Therefore the original state vector can also be replaced by, $\mathbf{x} = [V_N \ \theta]^T$ for system identification.

Based on the floating pendulum equations, it is expected that a model derived from $\dot{\theta}$ data will better approximate the actual dynamics than one using θ . This is because $\dot{\theta}$ is directly related to the dynamics, compared to θ which needs to be related to $\dot{\theta}$ to be relevant for the dynamics. However, an experiment to compare the performances of these models shows that this has a negligible effect.

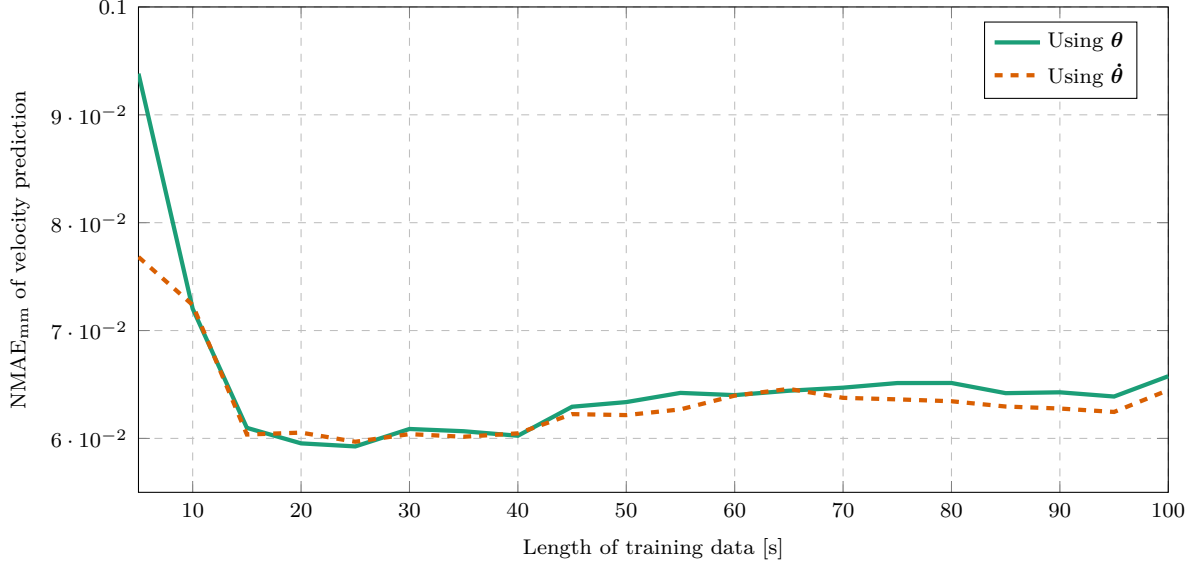


Figure 5.9: Prediction NMAE_{mm} for HAVOK models using either angle or angular rate measurements ($m = 0.2$ kg, $l = 1$ m, $T_s = 0.03$ s).

Figure 5.9 shows the prediction error of HAVOK models using $\dot{\theta}$ or θ for a range training data lengths. Only for very short lengths of training data, do models using $\dot{\theta}$ outperform those using θ . For longer lengths of training data there is a negligible difference in prediction error between the methods. Therefore θ will be used for system identification to avoid unnecessary complexity, since there is no direct measurement of $\dot{\theta}$ on the practical quadrotor.

5.6.6. Noise

Measurement noise is bad for system identification because it adds high frequency information to the output signals which are not part of the actual dynamics. On the practical quadrotor the IMU, barometer, magnetometer and GPS sensors experience measurement noise. The EKF performs sensor fusion and smooths out most of the measurement noise to provide a state estimate that is less noisy than raw sensor values. Therefore the output from the EKF is used for system identification.

The potentiometer and ADC which measure the payload angle on the quadrotor also has experience measurement noise. This signal is not smoothed by an onboard EKF. In simulation noise is applied to the payload angle as band-limited white-noise. The applied noise power was iteratively adjusted to match that of the practical payload measurements. The noisy signals from both the quadrotor EKF and payload swing angle are smoothed with a quadratic regression smoother from MATLAB[®] before applying system identification. The smoother uses a fixed window length of 20 samples which was selected iteratively to remove high frequency variation without losing the general shape of the data.

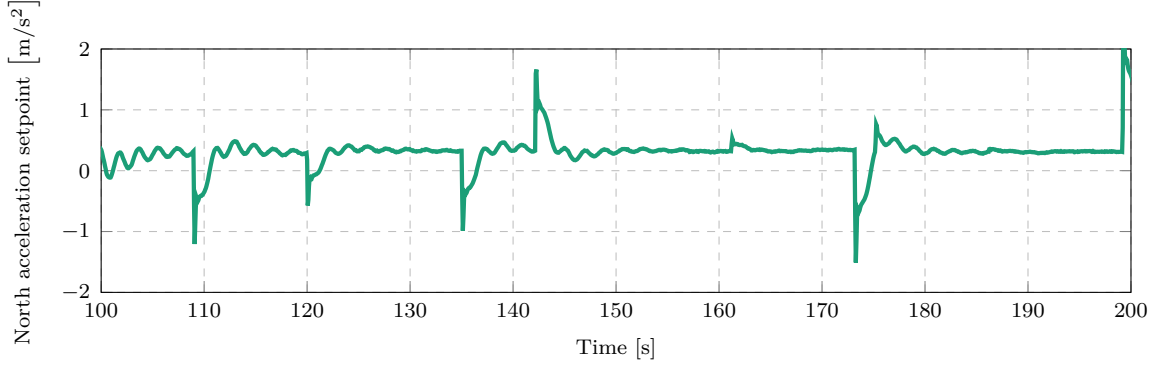


Figure 5.10: Acceleration setpoint training data from random velocity step inputs ($m = 0.2 \text{ kg}$, $l = 1 \text{ m}$)

The input signal also needs to be smoothed to remove high frequency noise from the logged signal. The quadratic regression smoother does not fit the shape of the input data well because of the sharp, non-differentiable edges in the acceleration setpoint signal. Therefore a Gaussian-weighted moving average smoother from MATLAB[®] is used for the input signal.

Figure 5.10 shows the North acceleration setpoint for a period of training data. Without noise the acceleration setpoint should have a zero mean, however the signal mean shows a constant offset. This is due to a measurement offset in the IMU which causes an offset in the orientation vector and therefore affects the control signals. The setpoint mean is calculated from the training data and subtracted from the signal to correct for the offset. This results in an input signal with a zero mean. The calculated mean is reapplied to the MPC control signal during implementation to readjust for the required offset.

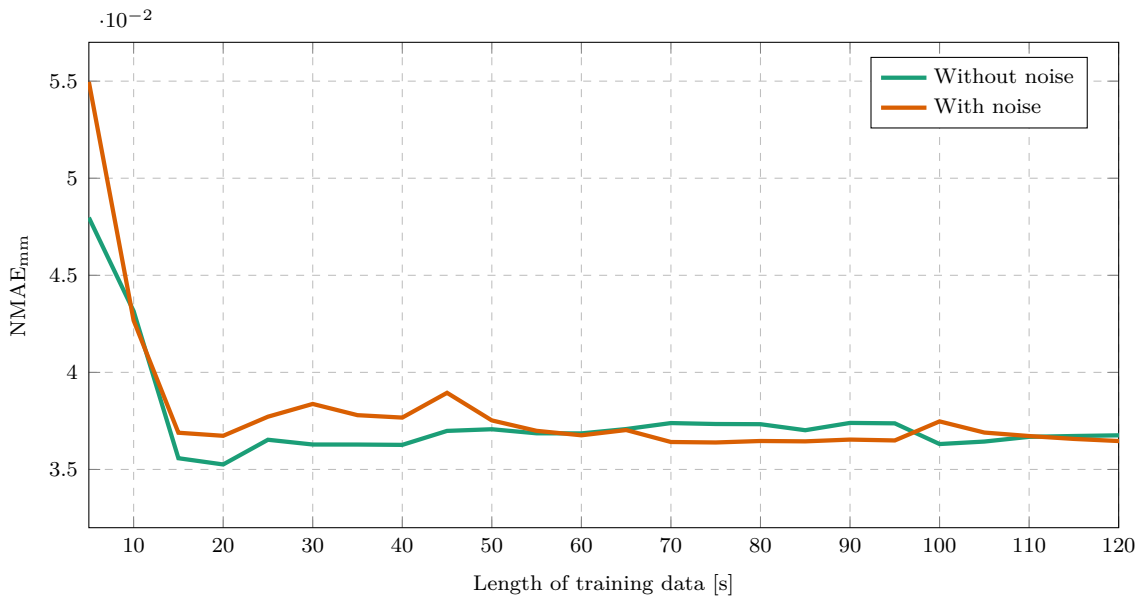


Figure 5.11: HAVOK prediction error for different lengths of training data with and without noise ($m = 0.2 \text{ kg}$, $l = 0.5 \text{ m}$, $T_s = 0.03 \text{ s}$).

Figure 5.11 compares the prediction errors of HAVOK models generated from data with or without noise. The plot shows that when using short lengths of training data, the prediction errors are smaller for model generated with noiseless signals. However, it appears that the prediction errors are almost equal with longer lengths of training data. This is because with a short length of data, the signal variation or energy contributed of the noise is a significant part of the data and has a strong influence on the model. However, with longer lengths of data, the variation caused by the actual plant dynamics dominates the low energy contribution of the measurement noise. Hence, the noise has a smaller influence on the model. It also appears that at long training data lengths noise has a negligible effect on the prediction error of the resulting models.

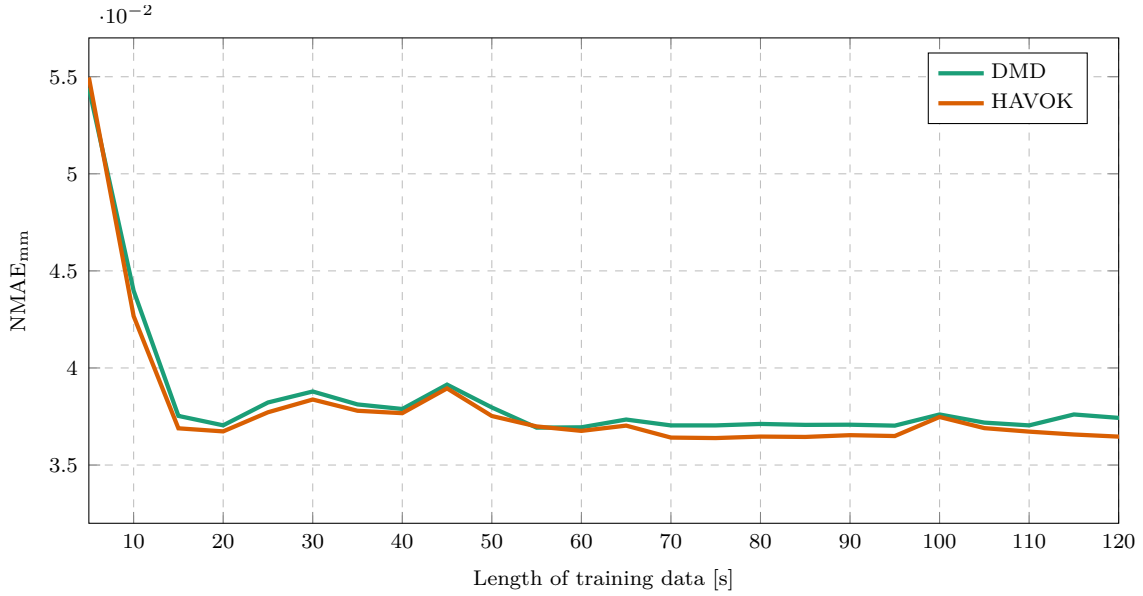


Figure 5.12: DMD and HAVOK prediction error for different lengths of noisy training data ($m = 0.2$ kg, $l = 0.5$ m, $T_s = 0.03$ s).

Figure 5.12 compares the performance of HAVOK and DMDc model when using noisy data. The prediction error curves of the two methods are very similar, with HAVOK producing slightly lower prediction errors than DMDc. However, this difference in error may be so small that it has a negligible effect on control.

5.6.7. System parameters

The suspended payload, as described in Section 5.2, has two system parameters, m_p and l . For the practical quadrotor considered, the payload mass is limited to, $0.1 \leq m_p \leq 0.3$ kg, and the cable length is limited to: $0.5 \leq l \leq 2$ m. Figure 5.13 shows the prediction error of HAVOK models build from simulations with various values of m_p and l . The plots are not shown for DMDc models because they are so similar to the HAVOK results.

From Figure 5.13a it seems that there is not a great difference in prediction error for different cable length setups. From Figure 5.13b it appears that m_p has a greater effect

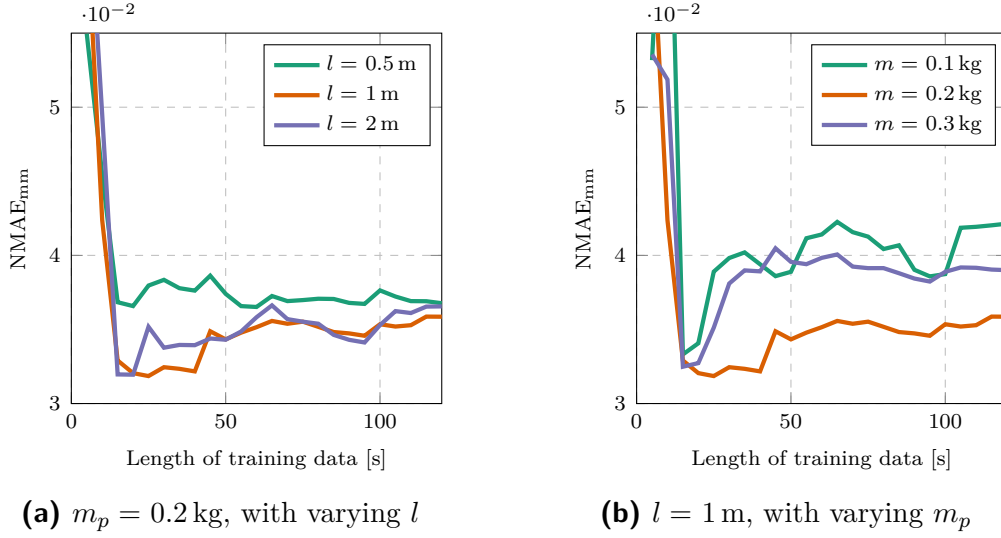


Figure 5.13: HAVOK prediction error for different system parameters

on prediction error, since there is a bigger difference in prediction error between plots of different m_p values. However, it is clear that the system identification method works for a range of different payload parameters.

5.6.8. Length of training data

From the plots discussed in previous sections, it is obvious that the accuracy of a model is dependant on the length of training data exposed to the system identification algorithm. The general relationship between length of training data and prediction error is illustrated in Figure 5.13. For very short lengths of training data the prediction error is large, but as training length increases, the prediction error improves up to a point. After this point, the prediction error slowly worsens with increasing lengths of training data.

This trend may be counter-intuitive, because it is generally expected that more training data leads to better models. The logic follows that more training data leads to less overfitting which leads to better test data predictions. However, a phenomenon named ‘double-descent’ occurs when the dimension of a regression model, D is near the number of training samples, N_{train} [23]. In this critical region at the transition between over-parameterized and under-parameterized models, the prediction error initially decreases, then increases to a peak whereafter it decreases again [23].

A rough calculation confirms that the critical region of ‘double-descent’ is applicable to our use case. The highest q in the considered range is 30, which corresponds to a model dimension of

$$D = (q \cdot n_x)^2 + (q \cdot n_x)(n_u) = 3660. \quad (5.23)$$

The length of training data corresponding to $D = N_{train} \cdot n_x$ at the transition between over- and under-parameterization is therefore:

$$T_{train} = N_{train} \cdot T_s = 54.9 \text{ s.} \quad (5.24)$$

This value is indeed within the range of considered training data lengths, which explains why our training experiments experience this phenomenon.

It should be noted that the plot for $l = 0.5 \text{ m}$ in Figure 5.13a does not follow the ‘double-descent’ trend. This may be because the short cable length corresponds to large swing angles and a high natural frequency. The onboard PID controllers do not damp these oscillations as quickly as the smaller angle and lower frequency oscillations of longer cables. Hence there is not enough information exposed in the first few step responses of the training data and the algorithm needs more step responses to accurately capture the steady-state behaviour of the plant.

In a practical implementations, training data is costly and it is desirable to use less training data. Less training data means less flight time will be wasted on training a model before the quadrotor can fly with a updated controller. Less training data also corresponds to lower memory usage on the quadrotor hardware and lower time-complexity for the algorithm. Therefore it is not practical to increase the amount of training data to the under-parameterized region. Hence, the critical region of training data lengths will be used and the data length corresponding to the lowest prediction error will be selected per simulation.

5.6.9. Dynamic payload

In Section 5.3 it was shown that the white-box system identification method perform well for the suspended payload use case. It was also shown in [2] and [1] that this method can be used in conjunction with LQR control to minimise swing angles of an unknown payload. However, many payloads do not satisfy the assumptions made in for the a priori model which is detrimental to performance of white-box method. For example, for an elongated payload attached to the cable the point mass assumption does not hold. The CoM of the payload is well below the attachment point of the cable, which creates a double pendulum model that differs significantly from a single pendulum. Such a payload is better represented in 2D by the double pendulum modelled in Figure 5.14, than the model defined in Figure 5.1.

Figure 5.15 shows the k-step-ahead prediction of a white-box models for a single pendulum simulation. The exact m_p is used for the model, but the cable length is estimated from a

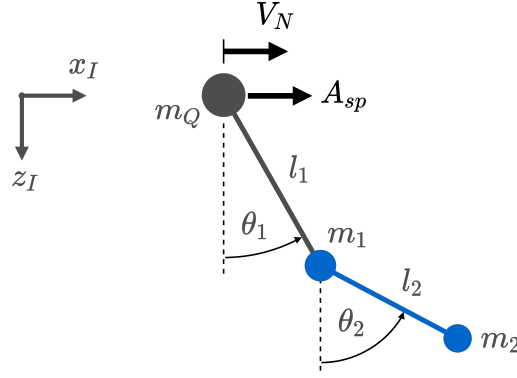


Figure 5.14: Double pendulum model representing an elongated suspended payload

FFT of the payload swing angle as described in Section 5.3.2. It is clear that the prediction is accurate for the first few oscillations, but the slight difference in frequency accumulates over time causing an increasingly large offset. However, the general shape of the dynamics is still captured by the model. Also note that the prediction oscillations are damped linearly but the actual oscillations experience non-linear damping. This difference is an approximation error because the non-linear plant is modelled with a linear model.

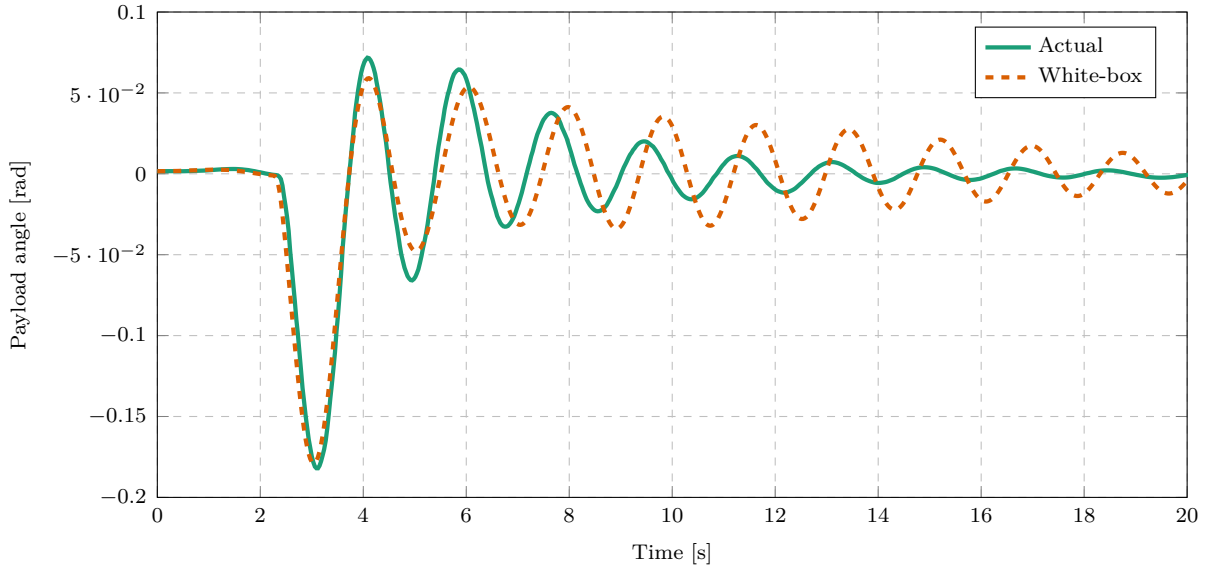


Figure 5.15: White-box model predictions of a single pendulum for a North velocity step input ($l = 1$ m, $m_p = 0.3$ kg.)

Figure 5.16 also shows the k-step-ahead prediction of a white-box model, but this prediction is for a double pendulum simulation. The cable length was estimated from the same method by calculating the FFT of the cable swing angle and identifying the dominant frequency. Note how the prediction of the first oscillation is quite accurate and is similar to the initial swing of the single pendulum. However, by the second swing, the double

pendulum dynamics differ significantly from the model prediction. The single pendulum oscillations seen in Figure 5.15 are regular compared to double pendulum oscillations in Figure 5.16 which are noticeably irregular. The a priori model expects regular, single frequency oscillations. This can be seen in Figure 5.16 where the predicted peaks are equidistant. However, the actual dynamics have a superposition of two frequencies due to the double pendulum payload.

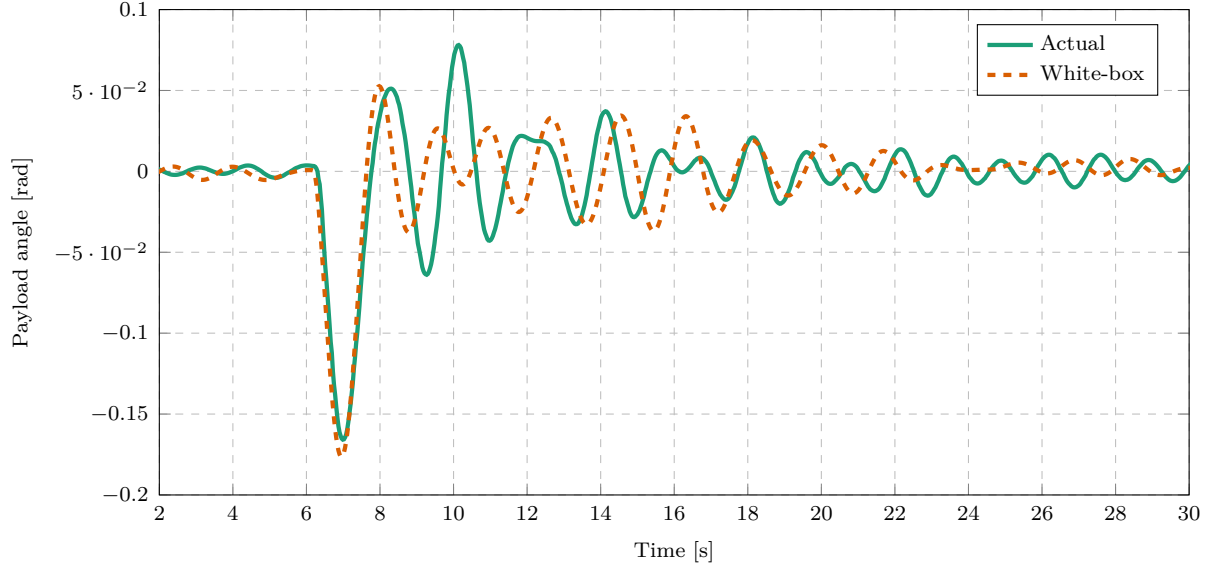


Figure 5.16: White-box model predictions of a double pendulum for a North velocity step input ($m = 0.3 \text{ kg}$, $l = 1 \text{ m}$)

The FFT amplitude spectrum of the single pendulum is shown in Figure 5.17b. This plot shows a single peak which corresponds to the natural frequency of the suspended payload. Figure 5.17a shows the FFT amplitude spectrum of the double pendulum. Two peaks are revealed in this plot which correspond to the two superimposed frequencies caused by the double pendulum. The frequency content of the two plants are clearly different so the white-box model and parameter estimation techniques would need to be redesigned for these payloads specifically. This is the great disadvantage of the white-box system identification technique. For every model with different dynamics, a new technique needs to be designed and used. In contrast, the proposed data-driven method provides a general solution for a large range of different payloads and dynamics.

Figure 5.18 shows the prediction of the two data-driven methods for a single pendulum simulation. Note that there is less of a frequency difference in this prediction than the white-box prediction in Figure 5.15. The shape of the predicted damping is also more similar to the actual dynamics than the white-box prediction. This may be because the data-driven methods effectively fit a higher order damping model to the dynamics, compared to the simple, linear damping applied in the white-box model.

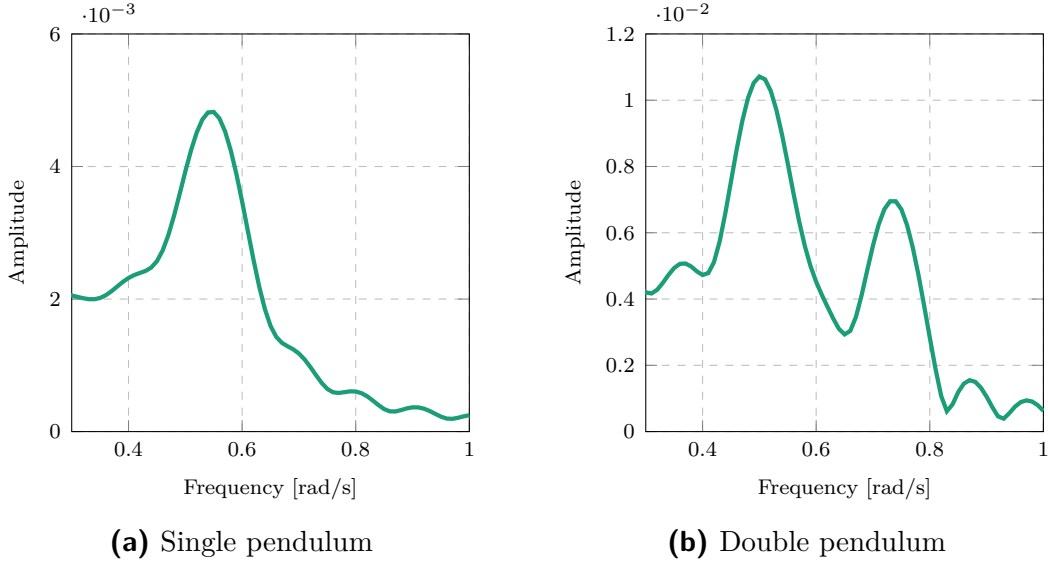


Figure 5.17: The single-sided amplitude spectrum of the swing angle FFT ($m = 0.3$ kg, $l = 1$ m).

The damping seen in these plots is a complicated effect which depends on the payload connection, the aerodynamic drag, and the controller gains. An advantage of data-driven system identification techniques is that the effect of damping is inherently included in the estimated model without specifically estimating a damping coefficient. In contrast, the white-box estimation technique requires the effect to be modelled a priori and a designed algorithm to estimate every parameter that effects the dynamics.

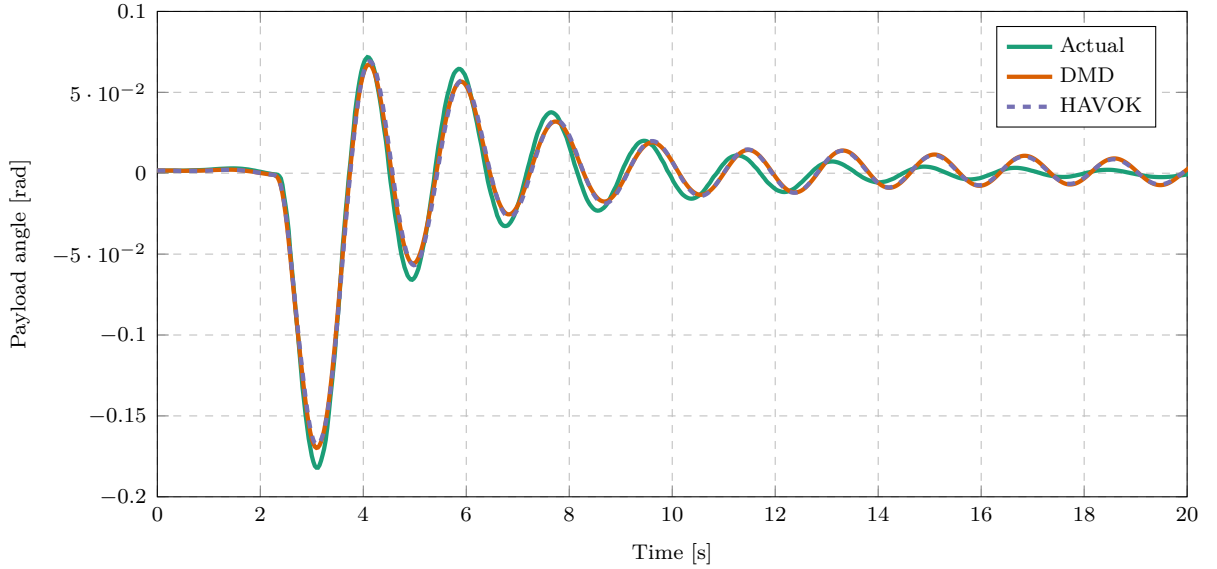


Figure 5.18: Data-driven model predictions of a single pendulum for a North velocity step input ($m_1 = 0.2$ kg, $l_1 = 1$ m, $m_2 = 0.1$ kg, $l_2 = 0.3$ m).

Figure 5.19 shows the prediction of the same data-driven methods but for a double pendulum simulation. The same cable length and effective payload mass is used here as in

the single pendulum simulation. Notice how accurate the prediction is for the first 20 s of the plot. In contrast to the white-box model, the black-box model oscillations follow the irregular, multi-frequency response of the actual dynamics. The state-space model can approximate the multi-frequency dynamics of the plant because of the delay-coordinates in the model. As expected, the prediction accuracy is also much better than the white-box models for both the single and double pendulum simulations.

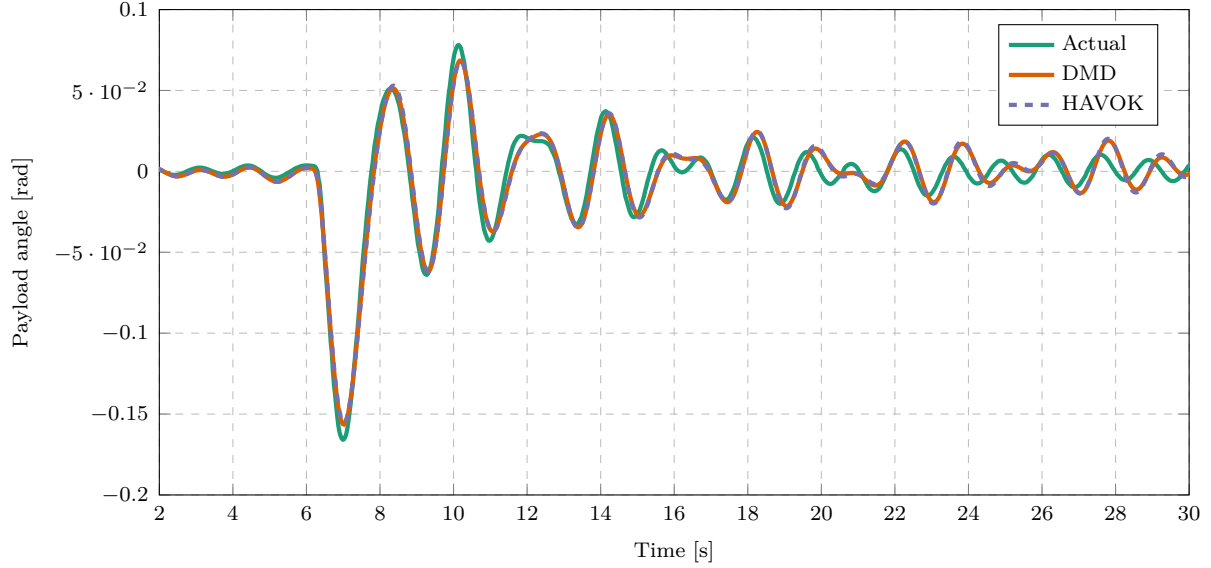


Figure 5.19: Data-driven model predictions of a double pendulum for a North velocity step input ($m_1 = 0.2$ kg, $l_1 = 1$ m, $m_2 = 0.1$ kg, $l_2 = 0.3$ m)

The double pendulum plant involves a hidden state variable, because the unmeasured angle of the second pendulum is required to fully describe the state of the system. However, the DMDc and HAVOK models are still able to approximate the dynamics quite accurately without measuring this state variable. This is due to the extent of the delay embedding of the models [14]. Figure 5.20 shows the prediction error as a function of the number of delays in the model for a double pendulum. Note how much more delays is required before the prediction error reaches steady-state than for a single pendulum showed in Figure 5.6. This is because the dynamics are more complex and model needs a lot more parameters to account for the hidden state variable.

Overall, the data-driven system identification approaches were shown to work well for both the single and double pendulum payloads. In contrast, the white-box method describes the general shape of the single pendulum dynamics well, but do not perform well for a double pendulum simulation because it was specifically designed for the single pendulum payload. The data-driven approaches therefore provide an accurate system identification method for a much larger range of payload types without needing a redesign for specific payload dynamics.

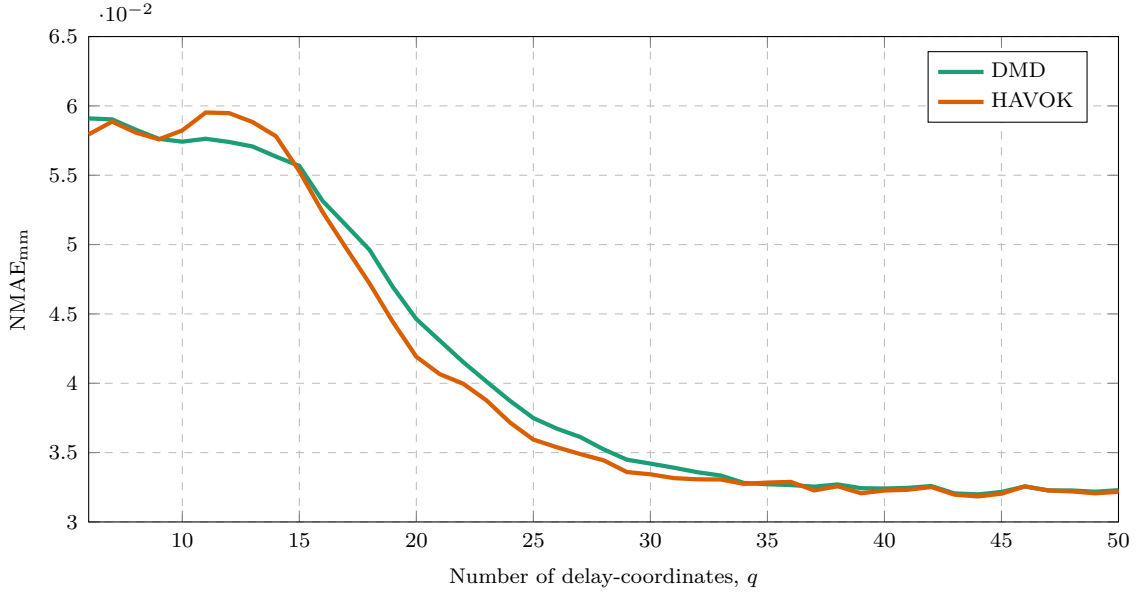


Figure 5.20: DMD and HAVOK predictions error of double pendulum for different numbers of delay-coordinates ($m_1 = 0.2 \text{ kg}$, $l_1 = 1 \text{ m}$, $m_2 = 0.1 \text{ kg}$, $l_2 = 0.3 \text{ m}$, $T_{train} = 70 \text{ s}$.)

5.7. Conclusion

DMDc and HAVOK produce very similar prediction errors for a range of different simulation conditions. HAVOK generally has slightly lower errors, but this may have a negligible effect on control. DMDc will be used in the remainder of this work because the algorithm has been studied more, is less computationally complex and provides similar performance to HAVOK. These data-driven methods were shown to produce accurate predictions of the payload dynamics with a practical length of training data, sample time and noise level. This proves to be promising for practical implementation with a MPC on a quadrotor companion computer. The data-driven methods also proved to provide accurate prediction with a range of different payload parameters and even with payloads that act as a double pendulum. In contrast, the considered white-box system identification technique failed to identify a relevant model for the double pendulum dynamics. Therefore the data-driven approach provides a more general system identification method that can be used for a range of different suspended payloads without being redesigned for specific dynamics.

Chapter 6

Control systems

6.1. Cascaded PID

Control system design Slower for less swing angles

6.2. LQR

Anton and Francois stuff

6.3. MPC

MATLAB QP solver C+ generation

Chapter 7

Implementation and results

7.1. LQR

7.2. MPC

7.3. Dynamic payload

7.4. System identification with practical data

7.5. HIL

Chapter 8

Summary and Conclusion

Bibliography

- [1] A. P. Erasmus and H. W. Jordaan, “Stabilization of a Rotary Wing Unmanned Aerial Vehicle with an Unknown Suspended Payload,” no. March, 2020.
- [2] J. F. Slabber and H. W. Jordaan, “Vision-Based Control of an Unknown Suspended Payload with a Multirotor Unmanned Aerial Vehicle,” Ph.D. dissertation, 2020.
- [3] S. L. Brunton, J. L. Proctor, and J. N. Kutz, “Discovering governing equations from data by sparse identification of nonlinear dynamical systems,” *Proceedings of the National Academy of Sciences*, vol. 113, no. 15, pp. 3932–3937, apr 2016. [Online]. Available: <https://www.pnas.org/content/113/15/3932><https://www.pnas.org/content/113/15/3932.abstract>
- [4] M. Bisgaard, A. La Cour-Harbo, and J. D. Bendtsen, “Input shaping for helicopter slung load swing reduction,” in *AIAA Guidance, Navigation and Control Conference and Exhibit*. American Institute of Aeronautics and Astronautics Inc., 2008. [Online]. Available: <https://arc.aiaa.org/doi/abs/10.2514/6.2008-6964>
- [5] J. H. Tu, C. W. Rowley, D. M. Luchtenburg, S. L. Brunton, and J. N. Kutz, “On dynamic mode decomposition: Theory and applications,” *Journal of Computational Dynamics*, vol. 1, no. 2, pp. 391–421, dec 2014. [Online]. Available: <https://www.aims sciences.org/article/doi/10.3934/jcd.2014.1.391>
- [6] J. L. Proctor, S. L. Brunton, and J. N. Kutz, “Dynamic mode decomposition with control,” *SIAM Journal on Applied Dynamical Systems*, vol. 15, no. 1, pp. 142–161, 2016.
- [7] M. Korda and I. Mezić, “Linear predictors for nonlinear dynamical systems: Koopman operator meets model predictive control,” *Automatica*, vol. 93, pp. 149–160, nov 2018. [Online]. Available: <http://arxiv.org/abs/1611.03537><http://dx.doi.org/10.1016/j.automatica.2018.03.046>
- [8] H. Arbabi, M. Korda, and I. Mezic, “A Data-Driven Koopman Model Predictive Control Framework for Nonlinear Partial Differential Equations,” *Proceedings of the IEEE Conference on Decision and Control*, vol. 2018-Decem, pp. 6409–6414, 2018.
- [9] C. M. Chen and K. H. Wang, “State-space model conversion of a system with state delay,” *Proceedings of the National Science Council, Republic of China, Part A: Physical Science and Engineering*, vol. 23, no. 6, pp. 782–788, 1999.

- [10] B. R. Noack, W. Stankiewicz, M. Morzyński, and P. J. Schmid, “Recursive dynamic mode decomposition of transient and post-transient wake flows,” *Journal of Fluid Mechanics*, vol. 809, pp. 843–872, 2016.
- [11] S. L. Brunton, B. W. Brunton, J. L. Proctor, E. Kaiser, and J. Nathan Kutz, “Chaos as an intermittently forced linear system,” *Nature Communications*, vol. 8, no. 1, dec 2017.
- [12] K. Champion, B. Lusch, J. N. Kutz, and S. L. Brunton, “Data-driven discovery of coordinates and governing equations,” *Proceedings of the National Academy of Sciences*, vol. 116, no. 45, pp. 22 445–22 451, nov 2019. [Online]. Available: <https://www.pnas.org/content/116/45/22445><https://www.pnas.org/content/116/45/22445.abstract>
- [13] S. L. Brunton and J. N. Kutz, *Data Driven Science & Engineering - Machine Learning, Dynamical Systems, and Control*, 2017. [Online]. Available: datatoolkit.uw.edu
- [14] M. Kamb, E. Kaiser, S. L. Brunton, and J. N. Kutz, “Time-Delay Observables for Koopman: Theory and Applications,” <https://doi.org/10.1137/18M1216572>, vol. 19, no. 2, pp. 886–917, apr 2020.
- [15] L. Meier, D. Honegger, and M. Pollefeys, “PX4: A node-based multithreaded open source robotics framework for deeply embedded platforms,” in *2015 IEEE International Conference on Robotics and Automation*. Institute of Electrical and Electronics Engineers Inc., jun 2015, pp. 6235–6240.
- [16] N. Koenig and A. Howard, “Design and use paradigms for Gazebo, an open-source multi-robot simulator,” *2004 IEEE/RSJ International Conference on Intelligent Robots and Systems (IROS)*, vol. 3, pp. 2149–2154, 2004.
- [17] J. Zhao, Y. Zhu, and R. Patwardhan, “Identification of k-step-ahead prediction error model and MPC control,” *Journal of Process Control*, vol. 24, no. 1, pp. 48–56, jan 2014.
- [18] R. J. Hyndman and A. B. Koehler, “Another look at measures of forecast accuracy,” *International Journal of Forecasting*, vol. 22, no. 4, pp. 679–688, oct 2006.
- [19] E. Kaiser, J. N. Kutz, and S. L. Brunton, “Sparse identification of nonlinear dynamics for model predictive control in the low-data limit,” *Proceedings of the Royal Society A: Mathematical, Physical and Engineering Sciences*, vol. 474, no. 2219, 2018.
- [20] N. M. Mangan, J. N. Kutz, S. L. Brunton, and J. L. Proctor, “Model selection for dynamical systems via sparse regression and information criteria,” *Proceedings of the Royal Society A: Mathematical, Physical and Engineering*

- Sciences*, vol. 473, no. 2204, p. 20170009, aug 2017. [Online]. Available: <https://royalsocietypublishing.org/doi/10.1098/rspa.2017.0009>
- [21] S. L. Brunton and J. N. Kutz, “Regression and Model Selection,” in *Data-Driven Science and Engineering*, 2019, vol. 1, pp. 117–153.
- [22] —, “Balanced Models for Control,” in *Data-Driven Science and Engineering*, 2019, pp. 321–344.
- [23] P. Nakkiran, G. Kaplun, Y. Bansal, T. Yang, B. Barak, and I. Sutskever, “Deep Double Descent: Where Bigger Models and More Data Hurt,” in *International Conference on Learning Representations*, 2020.

Appendix A

PID gains

This is an appendix about PID gains used for Honeybee.

Appendix B

Random appendix

This is another appendix.